

Article

Laser-Induced Tar-Mediated Sintering of Metals and Refractory Carbides in Air

Xining Zang, Kiera Y. Tai, Cuiying Jian, Wan Shou,
Wojciech Matusik, Nicola Ferralis, and Jeffrey C. Grossman

ACS Nano, **Just Accepted Manuscript** • DOI: 10.1021/acsnano.0c04295 • Publication Date (Web): 03 Aug 2020

Downloaded from pubs.acs.org on August 7, 2020

Just Accepted

“Just Accepted” manuscripts have been peer-reviewed and accepted for publication. They are posted online prior to technical editing, formatting for publication and author proofing. The American Chemical Society provides “Just Accepted” as a service to the research community to expedite the dissemination of scientific material as soon as possible after acceptance. “Just Accepted” manuscripts appear in full in PDF format accompanied by an HTML abstract. “Just Accepted” manuscripts have been fully peer reviewed, but should not be considered the official version of record. They are citable by the Digital Object Identifier (DOI®). “Just Accepted” is an optional service offered to authors. Therefore, the “Just Accepted” Web site may not include all articles that will be published in the journal. After a manuscript is technically edited and formatted, it will be removed from the “Just Accepted” Web site and published as an ASAP article. Note that technical editing may introduce minor changes to the manuscript text and/or graphics which could affect content, and all legal disclaimers and ethical guidelines that apply to the journal pertain. ACS cannot be held responsible for errors or consequences arising from the use of information contained in these “Just Accepted” manuscripts.

Laser-Induced Tar-Mediated Sintering of Metals and Refractory Carbides in Air

Xining Zang,¹ Kiera Y. Tai,¹ Cuiying Jian,^{1,2} Wan Shou,³ Wojciech Matusik,³ Nicola Ferralis,¹

Jeffrey C. Grossman^{1}*

¹ Department of Materials Science and Engineering, Massachusetts Institute of Technology, Cambridge, MA, 02139, USA

² Department of Mechanical Engineering, York University, 4700, Keele Street, Toronto, ON, M3J 1P3, Canada

³ Computer Science and Artificial Intelligence Laboratory, Massachusetts Institute of Technology, Cambridge, MA, 02139, USA

*Correspondence to email: jcg@mit.edu

ABSTRACT: Refractory Metals and their carbides possess extraordinary chemical and temperature resilience and exceptional mechanical strength. Yet, they are notoriously difficult to employ in additive manufacturing, due to the high temperatures needed for processing. State of the art approaches to manufacture these materials generally require either a high-energy laser or electron beam as well as ventilation to protect the metal powder from combustion. Here, we present a versatile manufacturing process that utilizes tar as both a light absorber and antioxidant binder

1
2
3 to sinter thin films of aluminum, copper, nickel, molybdenum, and tungsten powder using a low
4 power (< 2W) CO₂ laser in air. Films of sintered Al/Cu/Ni metals have sheet resistances of ~10⁻¹
5 ohm/sq, while laser sintered Mo/W-tar thin films form carbide phases. Several devices are
6 demonstrated, including laser sintered porous copper with a stable response to large strain (3.0)
7 after 150 cycles, and a laser processed Mo/MoC_(1-x) filament that reaches T~1000 °C in open air at
8 12 V. These results show that tar mediated laser sintering represents a possible low-energy, cost-
9 effective route for engineering refractory materials, and one that can easily be extended to additive
10 manufacturing processes.
11
12
13
14
15
16
17
18
19
20

21 KEYWORDS: steam cracker tar, laser sintering, transition metal, refractory metal carbides, laser
22 manufacturing
23
24
25
26
27
28
29
30
31
32

33 Refractory metals such as molybdenum, tungsten, and their carbides, possess extraordinary
34 chemical and thermal resilience and mechanical strength.^{1,2} Tungsten and molybdenum carbide
35 has been widely applied in machine tools and armor-piercing shells,³ and their alloys have been
36 applied in parts of aeronautical engines including nozzles and turbine blades.⁴ However, they can
37 be difficult to engineer due to their high melting temperature.⁵⁻⁷ Unlocking low-cost processing
38 conditions for sintering and printing methods using refractory materials could lead to additive
39 manufacturing processes and applications, from biomedical engineering,⁸ to power plants,⁹ to
40 aerospace.¹⁰
41
42
43
44
45
46
47
48
49
50
51

52 Laser annealing has been shown to provide low-cost versatile thermal processing methods with
53 broad material compatibility and spatial resolution.¹¹⁻¹⁴ In addition to controlling laser-specific
54
55
56
57
58
59
60

1
2
3 parameters such as power, rastering speed, and focus, material synthesis paradigms can be
4 developed by exploiting light-matter interactions to enhance and localize thermal
5 transformations.¹⁵ State-of-the-art additive manufacturing methods such as selective laser melting
6 (SLM) and electron beam melting (EBM) require relatively high laser power (up to several kW)
7 while operating under vacuum or inert gas.¹⁶ Direct additive manufacturing (3D printing) of
8 ceramics and refractory, high entropy alloys is generally difficult due to their high melting
9 temperature and the hardly controllable phase transformation during the thermal processes.^{10,17}
10 The current examples are still deployed by printing polymer based precursor followed by a post-
11 combustion process: silicon oxycarbide micro-lattice can be derived from preceramic polymers;
12 Al-Co-Cr-Fe-Ni alloy can be reduced by annealing in CO from 3D structure printed using polymer
13 blend with oxide nanopowder.^{7,18} These post-conversion processes induce volume shrinking,
14 porosity, and increase of impurities, and direct printing process will greatly help to resolve these
15 problems.

16
17
18
19
20
21
22
23
24
25
26
27
28
29
30
31
32
33
34 Herein, we present a versatile manufacturing process to sinter thin films of aluminum, copper,
35 nickel, molybdenum, and tungsten, using petroleum processing byproduct steam cracker tar (SCT)
36 as a binder.¹² The adaptable viscosity of tar, combined with its enhanced light absorption properties
37 and flexible chemistry, facilitates the direct patterning and laser sintering of metal microparticles
38 into metal and metal carbide thin films in air without formation of oxides. Using tar as a light
39 absorber and antioxidant enables direct sintering in air with a low power (< 2W) CO₂ laser, rather
40 than at the temperatures used in bulk annealing above melting temperatures (**Table S1**). Tar
41 displays an attenuation coefficient ($\sim 10^3 \text{ cm}^{-1}$) two orders of magnitude lower than that of metals
42 ($\sim 10^5 \text{ cm}^{-1}$) at the laser excitation wavelength (10.6 μm),^{19–22} resulting in a deeper penetration depth
43 of the laser into the metal-tar thin film. Additionally, the lower attenuation coefficient of tar allows
44
45
46
47
48
49
50
51
52
53
54
55
56
57
58
59
60

for higher efficiency in the photon to thermal energy conversion. By optimizing laser parameters and metal powder size distribution, we show that laser-treated metal/tar thin films produce metal phases (Al, Cu, Ni) and metal carbide phases (Mo, W) with low sheet resistance, as low as 10^{-1} ohm/sq. As proofs of concept, a printed copper auxetic pattern is transferred onto Ecoflex to assemble a strain sensor with a gauge factor of ~ 20 , and a printed molybdenum carbide thin film joule heater can reach over $1000\text{ }^{\circ}\text{C}$ in open air. Furthermore, we successfully demonstrate the tar-mediated sequential vertical patterning of a double layer molybdenum carbide thin film, which indicates the potential suitability of this method for additive manufacturing with refractory carbides.

RESULTS AND DISCUSSION

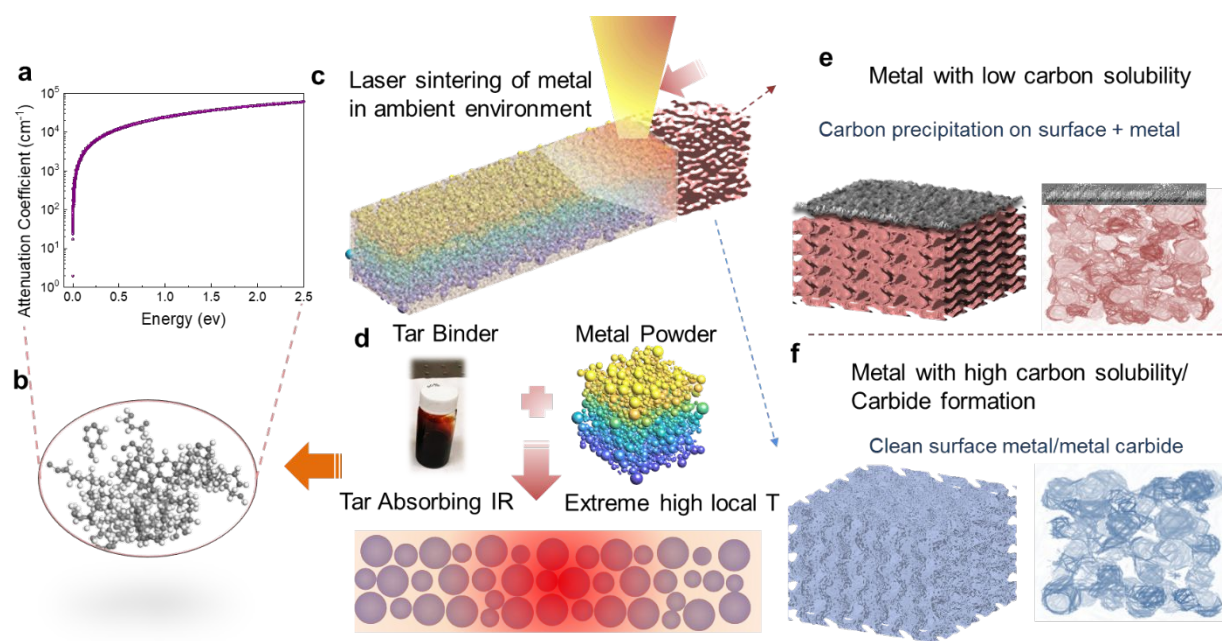


Figure 1 . Schematic of laser annealing of metal and refractory metal carbides using petroleum tar as the light-absorbing binder, at ambient conditions. (a) Attenuation coefficient of tar model calculated by first principles simulations. **(b)** Atomic model of tar. **(c-d)** Illustration of laser sintered metal thin film with tar binder. **(e)** Carbon segregation on metals with low carbon solubility like aluminum and copper after laser sintering. **(f)** Metals with high carbon solubility lead to a smooth surface after sintering; refractory metals molybdenum and tungsten form carbides.

1
2
3 Steam cracker tar, the byproduct of ethylene cracking, is a combination of polycyclic aromatic
4 hydrocarbons (PAHs) and alkanes (**Figure 1a-b**). Tar absorbs around 10 μm due to the C-C
5 vibration in PAH.²³ Using first principles simulations, the attenuation coefficient of tar at 10.6 μm
6 ($\sim 10^3 \text{ cm}^{-1}$), as shown in **Figure 1a-b** (for the details in **Figure S1** and **Table S2**) is found to be
7 much smaller than that of metals ($\sim 10^5 \text{ cm}^{-1}$) (**Table S1**). Carbon materials such sparse vertical
8 aligned carbon nanotube forest, carbon black and graphitic could function as near blackbody
9 materials to increase the light absorptivity and emissivity.²⁴ The heavy polyaromatics in tar are
10 transformed into a highly aromatic nano-scale framework during laser annealing, leading to the
11 formation of nano-scale cavities acting as black-bodies with near-unity absorptivity,¹² similarly
12 to nanoscale cavity absorption enhancements observed in carbon nanotubes.²⁴ Such structural
13 property could enhance the laser absorptivity and emissivity within the tar-metal and lead to a
14 higher internal temperatures. A tar solution (15 wt %) is made by diluting as received tar by
15 dichloromethane (DCM). Thin films are synthesized by spin coating from a suspension of metal
16 powder (1~5 μm particle size) in tar solution with mass ratio 100:15:85 (metal: tar: solvent)
17 (**Figure 1c-d**). The incident excitation laser incident power is found to be dissipated and reflected
18 internally among the metal particles, allowing it to penetrate deeper and increase the light/metal
19 power coupling.
20
21
22
23
24
25
26
27
28
29
30
31
32
33
34
35
36
37
38
39
40
41
42

43 As shown in **Figure 1e-f** and **Figure 2**, the structural conformation of sintered metal-tar thin
44 films depends on two factors: the carbon solid solubility in the given metal and the formation
45 energy of the corresponding metal carbide. In order to explore the roles of these two factors, five
46 metals of varying carbon solubility and carbide formation energies were chosen: Al, Cu, Ni, Mo
47 and W. Aluminum has both a relatively low melting temperature ($\sim 600 \text{ }^\circ\text{C}$) and low solid carbon
48 solubility (0.015 wt %). Copper also possesses a very low carbon solid solubility,²⁵ which has been
49
50
51
52
53
54
55
56
57
58
59
60

1
2
3 exploited to control the growth of monolayer graphene by chemical vapor deposition.²⁶ Ni has
4 high carbon solubility and strong chemisorption binding with carbon atoms.^{27,28} From the phase
5 diagram of Mo-C and W-C, the values of formation energy of their respective carbides are even
6 lower than melting Mo and W in the presence of carbon.^{29,30} (**Figure 2j,m** and **Figure S2-4**). Phase
7 segregation of carbon on the metal surface is not observed in laser annealed Ni-tar patterns from
8 SEM images, which can be attributed to the high carbon solid solubility of C in Ni. On the other
9 hand, a thin layer of amorphous carbon (<1/10 of film thickness) is always observed on the Cu-
10 based sintered film, as shown in the energy-dispersive X-ray spectroscopy (EDX) mapping and
11 Raman spectrum **Figure S2**. Similarly, a thin layer of carbon segregates to the surface of laser
12 sintered Al-tar thin films (**Figure S3**). We note that the intensity of the X-ray diffraction (XRD)
13 [2 0 0] reflection (52.4°, with a corresponding lattice distance of $d=2.02\text{\AA}$) increases with the
14 power/speed ratio indicating a recrystallization of Al powder in the laser sintering process. The
15 peak intensity ratio of $I_{d=2.02\text{\AA}}/I_{d=2.34\text{\AA}}$ of Al and laser sintered Al using 1% rastering speed
16 (12.7mm/s) and 8% power (~2.4 W) increases from 0.61 to 5.25, indicating a partial (~40 %)
17 recrystallization of Fm3m (FCC) phase cubic to Im3m (BCC) cubic Al derived from XRD
18 (**Figure S3b**). We note that no crystallization is ever observed for Cu, possibly due to the lower
19 internal temperature resulting from a lower carbon content within the carbon-metal interface and
20 with the metal particle itself. With an increase in power/rastering speed ratios, the restructured Al,
21 Cu and Ni coalition increases after sintering, rather than changing the chemical composition (such
22 as forming a carbide phase or oxides in air, **Figure S4**). The carbon residual in sintered Al, Cu,
23 and Ni thin film should be close to the carbon solid solubility in those metals.
24
25
26
27
28
29
30
31
32
33
34
35
36
37
38
39
40
41
42
43
44
45
46
47
48
49
50

51
52 The XRD patterns shown in **Figure 2j&m**, highlight the formation of carbide phases in both
53 laser-sintered Mo-tar and W-tar films. Higher incident laser power density (power/speed ratio) not
54
55
56
57
58
59
60

1
2
3 only increases the coalition size, but it also applies sufficiently high energy to induce the formation
4 of a mixed carbide/metal phase. Carbon in tar is over-saturated, which facilitates the formation of
5 metal carbide phases with either M_2C or $MC_{(1-x, 0 \leq x < 0.5)}$ stoichiometry. As shown in **Figure 2j-o** &
6 **3** and **Figure S5 & S6**, with the increase of projected power density, the lower energy β - Mo_2C
7 with lower formation temperature in the Mo-C phase diagram is observed as shown in the carbide
8 I regime. With further increase in incident power up to 2.4 W (at speed of 40 mm/s), a significant
9 amount (59 at%) of α - $MoC_{(1-x)}$ is observed as shown in the carbide II regime with 11 at% of
10 molybdenum metal. In the case of tungsten, lower energy phases δ -WC and α - $WC_{(1-x)}$ are observed
11 first. Using 12.7 mm/s as the fixed rastering speed, the β - W_2C phase starts to occur in the sintered
12 metal thin film using 0.9 W (3% of power). With higher incident power (>1.5 W), all carbides
13 exhibit the β - W_2C phase. With up to 2.1 W incident power, the sintered tungsten film has 62 at%
14 β - W_2C phase with 38 at% metal tungsten. It is worth noting that the carbide phases α - $MoC_{(1-x)}$ and
15 β - W_2C , which lie in the regime with higher metallurgical formation temperature, have higher
16 formation energy than the β - Mo_2C phase and δ -WC and α - $WC_{(1-x)}$ phases.
17
18
19
20
21
22
23
24
25
26
27
28
29
30
31
32
33
34
35
36
37
38
39
40
41
42
43
44
45
46
47
48
49
50
51
52
53
54
55
56
57
58
59
60

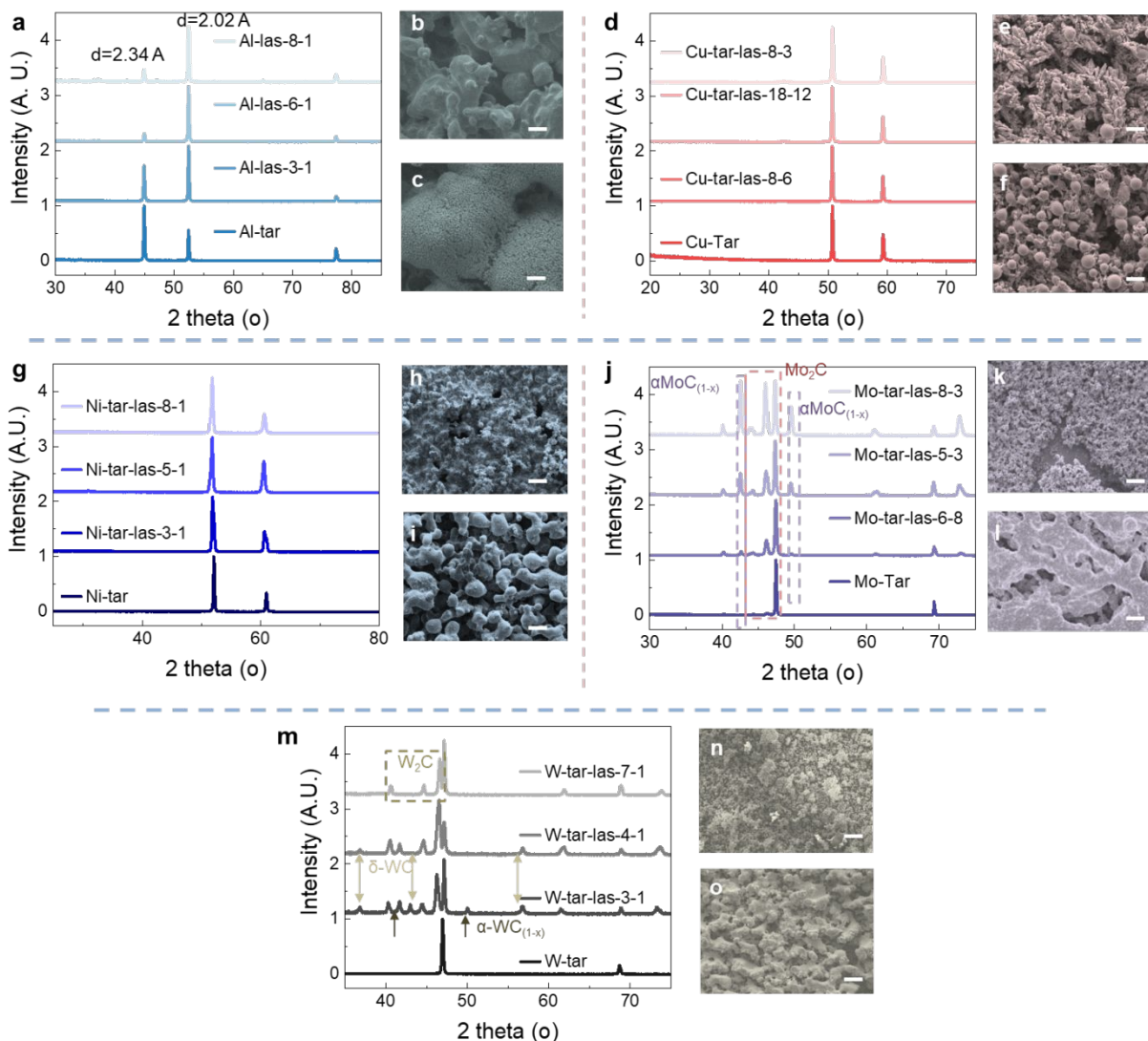


Figure 2. Laser sintered metal and refractory metal phases and microstructures. X-ray diffraction (XRD) pattern of laser-sintered metal-tar thin films and scanning electron micrograph (SEM) of as deposited and laser sintered metal-tar at different laser power and speed, for: (a-c) aluminum-tar; (d-f) copper-tar; (g-i) nickel-tar; (j-l) molybdenum-tar; (m-o) tungsten-tar. XRD in (a-c) shows the laser induced sintering leads to a preservation of the metal phases. XRD in (j) and (m) shows the laser sintering process leads to the formation of carbide phases. In (a,d,g,j,m) the first number after the “las-“label represents laser power and the second number represents speed in percentages. Scale bars: 10 μm .

Beside the crystallographic characterization of laser sintered metal/tar mixtures by XRD, electrical conductivities of sintered films are used to validate the formation of either metallic or carbide phases in refractory metals. Indeed, thin films show different trends in response to the ratio of incident laser power/speed, as shown in **Figure 3** and **Figure S7**. For aluminum, copper and

1
2
3 nickel thin films with tar, conductivities are primarily determined by the geometry and
4 connectivity of a percolated single metal phase. The lowest sheet resistance, $\sim 10^{-1}$ ohm/sq, can be
5 achieved by optimizing the laser power and rastering speed. As shown in **Figure 3** and **Figure S2-**
6
7
8
9
10
11
12
13
14
15
16
17
18
19
20
21
22
23
24
25
26
27
28
29
30
31
32
33
34
35
36
37
38
39
40
41
42
43
44
45
46
47
48
49
50
51
52
53
54
55
56
57
58
59
60

nickel thin films with tar, conductivities are primarily determined by the geometry and connectivity of a percolated single metal phase. The lowest sheet resistance, $\sim 10^{-1}$ ohm/sq, can be achieved by optimizing the laser power and rastering speed. As shown in **Figure 3** and **Figure S2-7**, metal-tar films are ablated by fixing either the laser power or rastering speed while varying the other. We define the power/scan speed ratio as rastering power density. **Figure 3d** illustrates the evolution of conductivities with power density. The evolution of metal phases and their microstructures, as well as the electrical conductivity of the resulting thin films follows directly from the incident rastering power density. High speeds and low power results in an “under ablation” regime, while higher power densities result in the increase in interparticle connectivity and conductivity of sintered metal patterns, leading to an optimal regime noted as “highest σ ” in **Figure 3c**. Further increases in rastering power density into the “over ablation” regime led to severe spheroidization of metal particles and a disconnected percolated network, due to the metal evaporation under high projected power density (**Figure S2-6**). For the formation of carbide phases, the relation between conductivity and power density is more nuanced. As shown in **Figure 3d**, the regimes of “under ablation” and “over ablation” are characterized by a rastering power density that is either too low to trigger sintering and recrystallization,³¹ or too high leading to a disruption in the metal percolation network. In the case of Mo and W, the increase of laser power and decrease of scan speed leads to formation of higher energy carbide phases (α -MoC_(1-x) and β -W₂C phase) with interparticle connectivity and thus increased conductivity (**Figure 3d**, **Figure S5-6**). The high conductivity regime is carbide II, and the conductivity increases while transitioning from carbide phase I to II. In the case of Mo, I-II refers to the β -Mo₂C to α -MoC_(1-x) transition. In the case of W, I-II refers to the α -WC_(1-x) to β -W₂C transition.

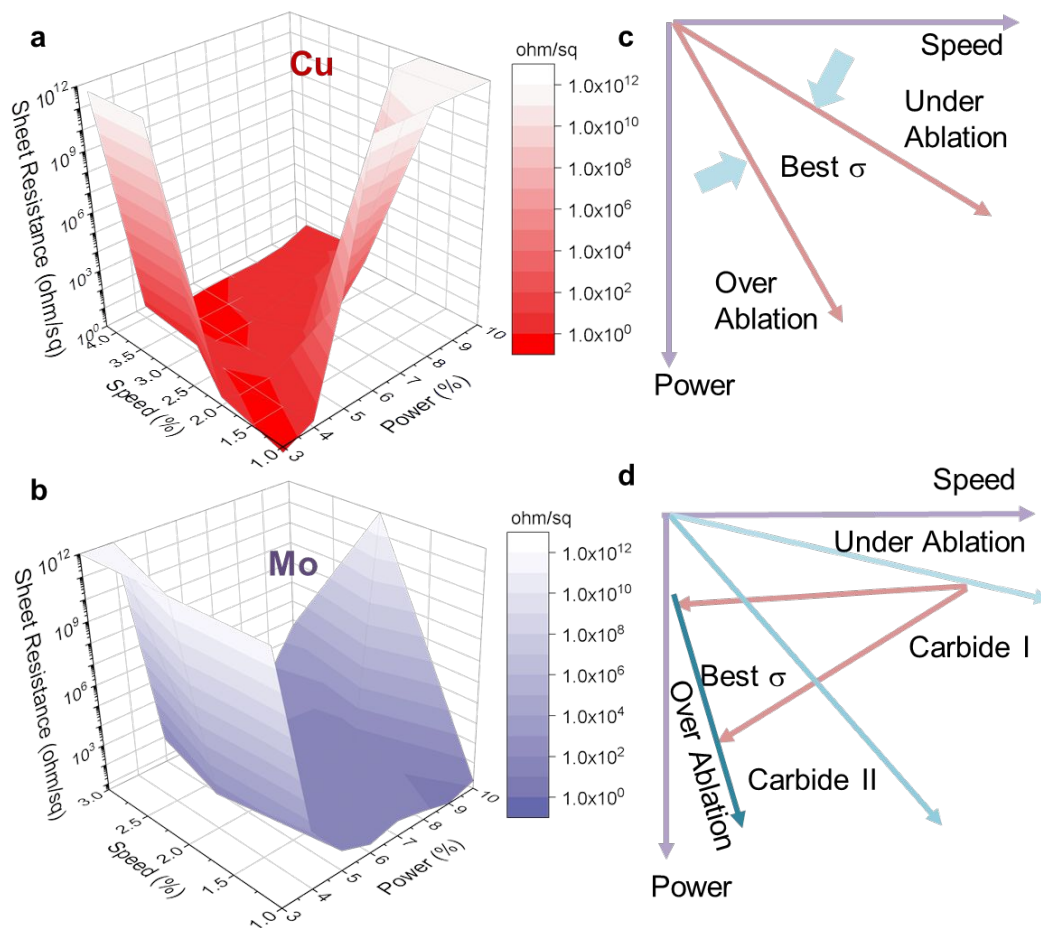


Figure 3. Electrical conductivities (σ) of laser annealed metal-tar thin films of (a) Cu-tar; (b) Ni-tar; Qualitative depiction of the evolution of: (c) non-carbide metal-tar thin films and (d) formation of carbide phases in refractory metal-tar thin films controlled by laser power and speed. Rastering speed (%) refers to the percentage to the maximum value (1270 mm/s), power (%) refers to the percentage of the full power (30W).

The initial size of metal powder in the metal-tar thin film is critical in determining the morphology and conductivity of the as-sintered metal thin film. As shown in **Figure S8a-c**, Mo-tar thin films are made from tar-metal solution with mass ratio 100:15:85 (metal: tar: solvent), using smaller powder size (~ 100 nm) following the same deposition and lasing processes for micro-size particles. Those thin films result in much higher sheet resistance (10^2 ohm/sq), while the lased thin film presents significantly deeper microfractures than laser-ablated Mo-tar using micron size powder (**Figure S8d-f**). The fractures can be attributed to the larger dewet induced

1
2
3 deformation and shrinking due to merging of particles in the laser sintered metal film, which could
4 be improved by increasing the packing density of metal powder in the tar-metal thin film. To
5 further increase the packing volume fraction³², we introduced metal powder with a smaller size
6 (~100nm) into the 1~5 μm size molybdenum powder with a mass ratio of 1:1 to make a Mo(mix)-
7 tar solution with the same mass ratio of tar and solvent in mono-size tar-metal solutions. Laser
8 sintered Mo(mix)-tar showed clear improvement compared to sintered Mo-tar using mono-
9 distributed micron size particles, displaying fewer visible cracks, and slightly lower sheet
10 resistance – decreased from 4.1 ohm/sq to 3.0 ohm/sq (**Figure S8g-i**).

11
12 We show next that devices can be fabricated through patterning using the optimized laser
13 parameters that give the highest conductivity (supplementary notes). Laser annealing with high
14 spatial resolution can be used to tailor the device geometry on temperature-sensitive substrates
15 such as polyimide. Residual un-lased copper-tar is washed off using dichloromethane (DCM)
16 (**Figure 4a**). The laser sintered copper pattern can be transferred onto flexible substrates such as
17 Ecoflex to fabricate stretchable electronic devices, in this case a strain sensor (**Figure 4b**). The
18 resistance of the as-printed auxetic pattern shows a linear response with applied strain up to 0.15,
19 with a gauge factor ~ 20 , which is much higher than the elasticity limit of copper metal.³³ The
20 auxetic pattern and the interconnected porous copper microstructures enables the repetitive
21 application of large strains beyond 150 cycles (**Figure S9**). Laser annealing a Mo/MoC_x in a wire
22 form-factor, shows low resistivity down to 0.5 ohm/sq, making it an ideal candidate for a Joule
23 heating filament.³⁴ **Figure 4c** shows that in such an application, the filament can reach up to ~ 1000
24 $^{\circ}\text{C}$ in open air with an input voltage of 12 V.

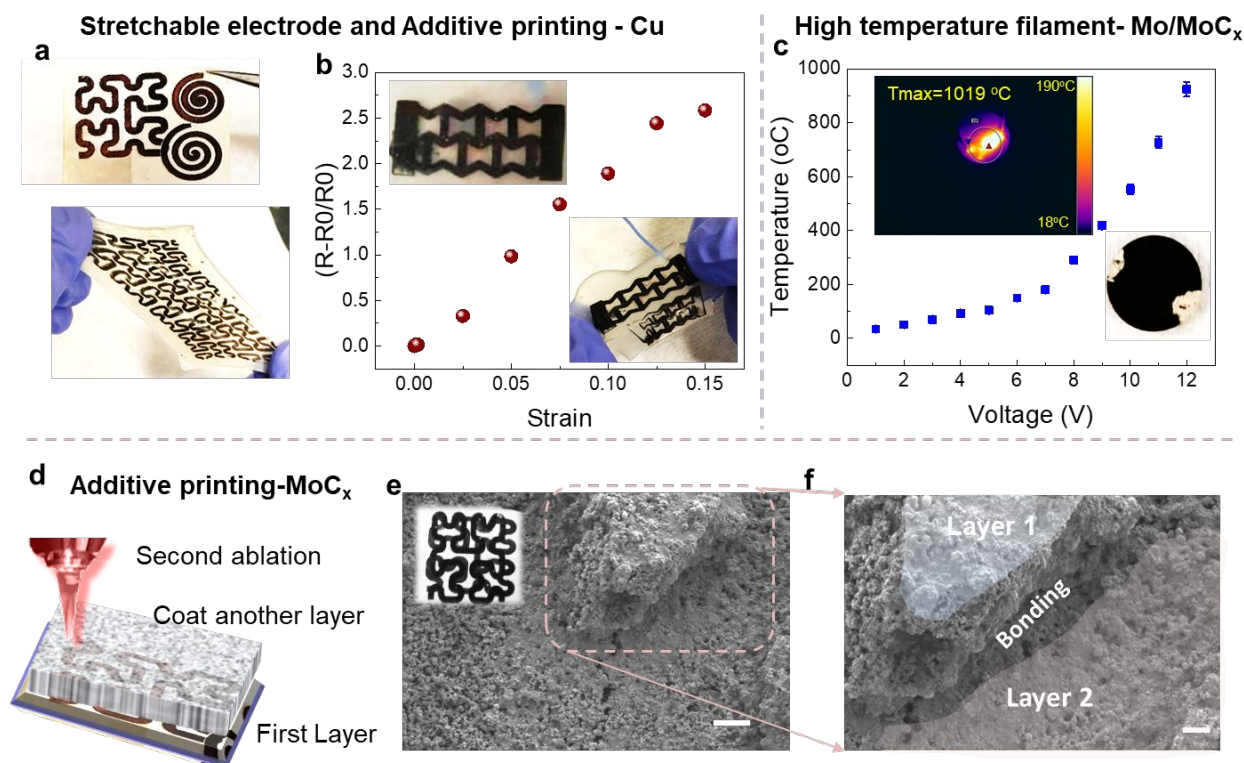


Figure 4. Application of laser annealed metal-tar microparticles for thin film electronics. (a) A pattern is printed on as-deposited Cu-tar film and transferred onto Ecoflex. (b) A strain sensor of auxetic copper pattern sandwiched between two layers of Ecoflex. (c) Maximum temperature values of Mo/MoC_x joule heating filament working in air corresponding as a function of input voltage. Inset, optical image of a joule heater printed on a quartz substrate with 0.5 inch diameter, with the temperature profile powered by a 12 V input voltage. The temperature color map was captured by the Infrared camera (FLIR). (d) Schematic of double layer metal printing using tar as absorption binder. (e) SEM image of printed double layer molybdenum carbide, with higher resolution area shown in (f) highlighting the bonding interface between two vertical layers. Scale bar in (e) and (f): 50 μ m and 20 μ m.

The viability of the laser sintering process in additive manufacturing is tested by synthesizing a vertical sintered double layer. Here, a layer-by-layer coating and printing is achieved through repeated sequences of depositions, patterning, laser annealing and residual washing off. While residual carbon on the laser sintered Cu and Al thin films will block the formation of interlayer bonding, carbide formation in Mo-tar and W-tar could potentially bond the two layers. As a proof-of-concept, a double layer of a Mo/MoC_x pattern is demonstrated in **Figure 4d-f**. After removing the residual powder, the bonding between the two layers of Mo/MoC_x can be seen from the SEM

1
2
3 of **Figure 4f**. The first layer molybdenum sintering is performed using low power (1.8 W) and low
4
5 rastering speed (12.7 mm/s) to increase the packing density of the sintered structure. The second
6
7 layer is sintered with relatively high power (~4.5 W) and a rastering speed of (101.6 mm/s) to
8
9 increase the penetration depth and interlayer bonding. Such a result indicates the potential of
10
11 extending the tar mediated laser sintering of metal carbide formation into additive printing
12
13 processes.
14
15

16 17 18 CONCLUSION

19
20
21 In summary, we present tar-mediated laser sintering of metal nano- and microparticles including
22
23 Al, Cu, Ni, and refractory Mo and W using relatively low power (< 2 W) under ambient conditions.
24
25 A thin layer of carbon segregates on aluminum and copper sintered films surface due to its low
26
27 solubility in these metals,²⁵ while nickel with higher carbon solubility provides a clean surface
28
29 after laser annealing.²⁸ Refractory metals (molybdenum and tungsten) which are laser sintered in
30
31 air, result in different high energy transition metal carbide phases,^{29,30} through optimized control
32
33 over laser power and rastering speed. By exploiting the microstructure and high electrical
34
35 conductivity of the laser sintered metal and metal carbide thin films, we demonstrate the successful
36
37 fabrication of a strain sensor with a laser-printed copper auxetic pattern with linearity behavior up
38
39 to 15% strain, and a gauge factor of ~20. Laser printed Mo/MoC_x Joule heating filaments are also
40
41 fabricated with a sheet resistance below 1.6 ohm/sq, leading to an operational maximum
42
43 temperature over 1000 °C in the open air with an input power of 12 V. Furthermore, we
44
45 demonstrated a proof-of-concept sequential multi-layer printing process of molybdenum carbide,
46
47 with a method that can be potentially expanded and integrated into additive manufacturing
48
49 processes.
50
51
52
53
54
55
56
57
58
59
60

1
2
3 Most importantly, with the assistance of an absorbing binder the input energy is two orders of
4 magnitude smaller than what is required in other metal printing methods such as selective laser
5 melting (SLM),^{4,35,36} and electron beam melting (EBM).^{37,38} Without using tar in the metal thin
6 film, the low power down to 1W cannot trigger any photon-induced thermal reactions.
7
8 Furthermore, the laser-induced metal sintering method here proposed operates under ambient
9 conditions, eliminating the need for ventilation and pumping, in turn decreasing the processing
10 time and complexity compared to SLM and EBL. Direct laser printing in air through a compact
11 laser source reduces the processing overhead imposed by the otherwise required control over the
12 buffer gas during annealing and instrumentational complexity in the case of EBM. Such factors
13 could potentially reduce the complexity of fabricating metal and metal carbide films in continuous
14 “roll-to-roll” manufacturing. Furthermore, the tar-metal ink could potentially be adapted to an
15 extrusion-based 3D printer with fiber optics, and thus be done in an additive way of printing.
16
17
18
19
20
21
22
23
24
25
26
27
28
29
30

31 MATERIALS AND METHODS

32 **Materials**

33
34 Stream cracked tar was provided by ExxonMobil (Defluxed SOP2 Tar from 15-082837).
35
36 Aluminum powder (1~5 μm) and copper powder (<45 μm) were purchased from Sigma Aldrich.
37
38 nickel powder (3~7 μm), molybdenum powder (2~4 μm), and tungsten powder (1~5 μm) were
39
40 all purchased from Alfa Aesar. Dichloromethane (DCM, CAS 75-09-2) was purchased from Sigma
41
42 Aldrich.
43
44
45
46
47
48

49 **Materials Analysis and Characterization**

50
51 A profilometer (Bruker DXT Stylus Profilometer) was used to map the thickness of spin coated
52
53 and laser ablated thin films. Scanning electron microscopy (SEM, Hitachi SU8100) was used to
54
55 image the laser sintered metal-tar thin films. Energy-dispersive X-ray spectroscopy (EDX)
56
57
58
59
60

1
2
3 mapping was taken in SEM using an Oxford EDX detector (15 kV, 20 μm) controlled by an APEX
4 software interface. Micro-Raman spectra were acquired using a Renishaw inVia™ confocal
5 Raman microscope using a 473 nm excitation source. The laser spot on the sample was ~ 800 nm
6 in diameter and had a power of ~ 4 mW at the sample surface. The full spectral window for each
7 acquisition is from 600 to 3200 cm^{-1} . X-ray diffraction patterns of metal-tar thin films were tested
8 using the Bruker D8 Discovery, and semi-quantitative analysis of patterns was performed using
9 HighScore software to identify the phases and estimate the components.

20 **Laser Sintering of Metal-tar Thin Film**

21
22 A tar solution (15 wt%) was made by diluting as received tar by dichloromethane (DCM). Thin
23 films were created by spin coating a suspension of metal powder in the tar solution with mass ratio
24 100:15:85 (metal: tar: solvent). Metal powders and their physical properties are summarized in
25 tab. S1. The tar solution was spun coated onto glass substrates at a speed of 500 rpm for 20 seconds,
26 and the deposited metal-tar thin films were dried in air for 4 hours and heated up to 80 $^{\circ}\text{C}$ to remove
27 the volatile component and residual solvent. A commercial laser cutter (Universal VSL 2.30) was
28 utilized to perform the laser annealing and sintering, with a CO_2 laser tube (maximum power of
29 30W) and all built-in optics. The laser spot was focused on the top surface of the spin-coated films
30 by tuning the z-position (height) of the supporting cutting table. The designed pattern was imported
31 to a vector graphics software (Inkscape) and engraved by communicating with the laser cutter as
32 a printer. On different metal-tar thin films, different parameters of power and speed were crossed
33 compared for maximum conductivity at focus.

51 **Prototyping Laser Sintered Metal Devices**

52
53 To prototype more complex designs for metal devices, the laser was calibrated to the parameters
54 that achieved the highest conductivity. Using a computer aid design (CAD) interface, many
55

1
2
3 features were directly printed on tar-metal film. As-ablated devices were rinsed in solvent DCM
4
5 to remove the unablated areas, and air dried followed with heat up to 100 °C to fully remove
6
7 solvent. Copper-tar printed in the patterns in Figure 4a are sintered by laser annealing and washed
8
9 with solvent to remove residual copper powder and transferred onto Ecoflex to make a stretchable
10
11 strain sensor.
12
13

14 15 **Conductivity Measurement**

16
17 A lakeshore TTP4 probe station was used for sheet resistance characterization. Parameter
18
19 analyzer (4156C) is interfaced with a PC running EasyExpert software to setup any test with up to
20
21 1mA and 5V. All room temperature electrical characterization was done under air.
22
23
24

25 26 **Testing of the Mo/MoC_{1-x} filament**

27
28 Mo-tar thin films were deposited onto quartz substrates of 0.5-inch diameter. Laser sintering
29
30 was performed as described above with the calibrated power and speed parameters with the highest
31
32 resulting conductivity. Two electrodes were deposited using silver paste on the edge of the
33
34 Mo/MoC_x thin film. The heating performance of the filament was tested using a DC voltage source,
35
36 ranging from 1-12 V with a step of 1 V. At each voltage input, the temperature was recorded by
37
38 an IR camera (FLIR A 615) for 10 min until the temperature saturated.
39
40
41

42
43 ASSOCIATE CONTENT

44 45 **Supporting Information**

46
47 The Supporting Information is available free of charge at xxxx;

48
49 The Supplementary materials includes:

50
51 Physical and optical properties of tar and metals tested, simulation set up of tar, SEMs of
52
53 laser sintered metal-tar thin films, conductivities (σ) of laser annealed metal-tar thin films, and a
54
55 demonstration of strain sensor made of laser sintered copper.
56
57
58
59
60

1
2
3 AUTHOR INFORMATION
4
5

6 **Corresponding Author**
7

8 * Jeffrey. C. Grossman, email: jcg@mit.edu
9
10

11
12 **Author Contributions**
13

14 X.Z. and J.C.G. designed the research; X.Z. designed and performed experiments; K.Y.T. helped
15 with metal sintering; C. J. performed the simulation; W.S. helped with the test of printed sensors;
16
17 N.F. provided insight on tar chemistry, film and process characterization; X.Z., N.F. and J.C.G.
18
19 wrote the paper; all the authors provided comments and feedback on the manuscript.
20
21
22
23
24
25

26 **ACKNOWLEDGMENT**
27

28 The Tar used in this work was provided by ExxonMobil. All authors claim no competing interests.
29
30 This work made use of the MRSEC Shared Experimental Facilities at MIT, supported by the
31
32 National Science Foundation under award number DMR-14-19807.
33
34
35
36
37
38
39
40
41
42

43 **REFERENCES**
44
45
46

- 47 (1) Antusch, S.; Reiser, J.; Hoffmann, J.; Onea, A. Refractory Materials for Energy
48 Applications. *Energy Technol.* **2017**, *5*, 1064–1070.
49
50
51 (2) Pierson, H. O. Carbides of Group VI. In *Handbook of Refractory Carbides and Nitrides*;
52 William Andrew Inc: New York, 1996; pp 100–117.
53
54
55
56 (3) Prakash, L. J. Application of Fine Grained Tungsten Carbide Based Cemented Carbides.
57
58
59
60

- 1
2
3 *Int. J. Refract. Met. Hard Mater.* **1995**, *13*, 257–264.
4
5
6 (4) Mercelis, P.; Kruth, J. Residual Stresses in Selective Laser Sintering and Selective Laser
7 Melting. *Rapid Prototyp. J.* **2006**, *12*, 254–265.
8
9
10 (5) Visser, C. W.; Pohl, R.; Sun, C.; Römer, G.-W.; Huis in 't Veld, B.; Lohse, D. Toward 3D
11 Printing of Pure Metals by Laser-Induced Forward Transfer. *Adv. Mater.* **2015**, *27*, 4087–
12 4092.
13
14
15
16 (6) Wang, Y. M.; Voisin, T.; McKeown, J. T.; Ye, J.; Calta, N. P.; Li, Z.; Zeng, Z.; Zhang, Y.;
17 Chen, W.; Roehling, T. T.; Ott, R. T.; Santala, M. K.; Depond, P. J.; Matthews, M. J.;
18 Hamza, A. V.; Zhu, T. Additively Manufactured Hierarchical Stainless Steels with High
19 Strength and Ductility. *Nat. Mater.* **2018**, *17*, 63–71.
20
21
22
23 (7) Kenel, C.; Casati, N. P. M.; Dunand, D. C. 3D Ink-Extrusion Additive Manufacturing of
24 CoCrFeNi High-Entropy Alloy Micro-Lattices. *Nat. Commun.* **2019**, *10*, 904.
25
26
27
28 (8) Prasad, K.; Bazaka, O.; Chua, M.; Rochford, M.; Fedrick, L.; Spoor, J.; Symes, R.; Tieppo,
29 M.; Collins, C.; Cao, A.; Markwell, D.; Ostrikov, K. (Ken); Bazaka, K. Metallic
30 Biomaterials: Current Challenges and Opportunities. *Materials.* **2017**, *10*, 884.
31
32
33
34 (9) Antusch, S.; Reiser, J.; Hoffmann, J.; Onea, A. Refractory Materials for Energy
35 Applications. *Energy Technol.* **2017**, *5*, 1064–1070.
36
37
38
39 (10) Penilla, E. H.; Devia-Cruz, L. F.; Wieg, A. T.; Martinez-Torres, P.; Cuando-Espitia, N.;
40 Sellappan, P.; Kodera, Y.; Aguilar, G.; Garay, J. E. Ultrafast Laser Welding of Ceramics.
41 *Science (80-.).* **2019**, *365*, 803–808.
42
43
44
45 (11) El-Kady, M. F.; Kaner, R. B. Scalable Fabrication of High-Power Graphene Micro-
46 Supercapacitors for Flexible and on-Chip Energy Storage. *Nat. Commun.* **2013**, *4*, 1475.
47
48
49
50 (12) Zang, X.; Jian, C.; Ingersoll, S.; Li, H.; Adams, J. J.; Lu, Z.; Ferralis, N.; Grossman, J. C.
51 Laser-Engineered Heavy Hydrocarbons: Old Materials with New Opportunities. *Sci. Adv.*
52 **2020**, *6*, eaaz5231.
53
54
55
56
57
58
59
60

- 1
2
3 (13) Tan, K. W.; Jung, B.; Werner, J. G.; Rhoades, E. R.; Thompson, M. O.; Wiesner, U.
4 Transient Laser Heating Induced Hierarchical Porous Structures from Block Copolymer–
5 Directed Self-Assembly. *Science (80-.)*. **2015**, *349*, 54–58.
6
7
8
9 (14) Zang, X.; Jian, C.; Zhu, T.; Fan, Z.; Wang, W.; Wei, M.; Li, B.; Follmar Diaz, M.; Ashby,
10 P.; Lu, Z.; Chu, Y.; Wang, Z.; Ding, X.; Xie, Y.; Chen, J.; Hohman, J. N.; Sanghadasa, M.;
11 Grossman, J. C.; Lin, L. Laser-Sculptured Ultrathin Transition Metal Carbide Layers for
12 Energy Storage and Energy Harvesting Applications. *Nat. Commun.* **2019**, *10*, 3112.
13
14
15 (15) Zang, X.; Shen, C.; Chu, Y.; Li, B.; Wei, M.; Zhong, J.; Sanghadasa, M.; Lin, L. Laser-
16 Induced Molybdenum Carbide–Graphene Composites for 3D Foldable Paper Electronics.
17 *Adv. Mater.* **2018**, *30*, 1800062.
18
19
20 (16) Frazier, W. E. Metal Additive Manufacturing: A Review. *J. Mater. Eng. Perform.* **2014**, *23*,
21 1917–1928.
22
23
24 (17) Wu, D.; Liu, H.; Lu, F.; Ma, G.; Yan, S.; Niu, F.; Guo, D. Al₂O₃-YAG Eutectic Ceramic
25 Prepared by Laser Additive Manufacturing with Water-Cooled Substrate. *Ceram. Int.* **2019**,
26 *45*, 4119–4122.
27
28
29 (18) Eckel, Z. C.; Zhou, C.; Martin, J. H.; Jacobsen, A. J.; Carter, W. B.; Schaedler, T. A.
30 Additive Manufacturing of Polymer-Derived Ceramics. *Science (80-.)*. **2016**, *351*, 58–62.
31
32
33 (19) Babar, S.; Weaver, J. H. Optical Constants of Cu, Ag, and Au Revisited. *Appl. Opt.* **2015**,
34 *54*, 477.
35
36
37 (20) Ordal, M. A.; Bell, R. J.; Alexander, R. W.; Long, L. L.; Querry, M. R. Optical Properties
38 of Fourteen Metals in the Infrared and Far Infrared: Al, Co, Cu, Au, Fe, Pb, Mo, Ni, Pd, Pt,
39 Ag, Ti, V, and W. *Appl. Opt.* **1985**, *24*, 4493.
40
41
42 (21) Ordal, M. A.; Long, L. L.; Bell, R. J.; Bell, S. E.; Bell, R. R.; Alexander, R. W.; Ward, C.
43 A. Optical Properties of the Metals Al, Co, Cu, Au, Fe, Pb, Ni, Pd, Pt, Ag, Ti, and W in the
44 Infrared and Far Infrared. *Appl. Opt.* **1983**, *22*, 1099.
45
46
47 (22) Ordal, M. A.; Bell, R. J.; Alexander, R. W.; Newquist, L. A.; Querry, M. R. Optical
48
49
50
51
52
53
54
55
56
57
58
59
60

- 1
2
3 Properties of Al, Fe, Ti, Ta, W, and Mo at Submillimeter Wavelengths. *Appl. Opt.* **1988**,
4 27, 1203.
5
6
7
8 (23) Alcañiz-Monge, J.; Cazorla-Amorós, D.; Linares-Solano, A. Characterisation of Coal Tar
9 Pitches by Thermal Analysis, Infrared Spectroscopy and Solvent Fractionation. *Fuel* **2001**,
10 80, 41–48.
11
12
13
14 (24) Mizuno, K.; Ishii, J.; Kishida, H.; Hayamizu, Y.; Yasuda, S.; Futaba, D. N.; Yumura, M.;
15 Hata, K. A Black Body Absorber from Vertically Aligned Single-Walled Carbon
16 Nanotubes. *Proc. Natl. Acad. Sci.* **2009**, 106, 6044–6047.
17
18
19
20 (25) López, G. A.; Mittemeijer, E. J. The Solubility of C in Solid Cu. *Scr. Mater.* **2004**, 51, 1–5.
21
22
23 (26) Li, X.; Cai, W.; An, J.; Kim, S.; Nah, J.; Yang, D.; Piner, R.; Velamakanni, A.; Jung, I.;
24 Tutuc, E.; Banerjee, S. K.; Colombo, L.; Ruoff, R. S. Large-Area Synthesis of High-Quality
25 and Uniform Graphene Films on Copper Foils. *Science (80-.)*. **2009**, 324, 1312–1314.
26
27
28
29 (27) Klinke, D. J.; Wilke, S.; Broadbelt, L. J. A Theoretical Study of Carbon Chemisorption on
30 Ni(111) and Co(0001) Surfaces. *J. Catal.* **1998**, 178, 540–554.
31
32
33
34 (28) Singleton, M.; Nash, P. The C-Ni (Carbon-Nickel) System. *Bull. Alloy Phase Diagrams*
35 **1989**, 10, 121–126.
36
37
38 (29) Hugosson, H. W.; Eriksson, O.; Nordström, L.; Jansson, U.; Fast, L.; Delin, A.; Wills, J.
39 M.; Johansson, B. Theory of Phase Stabilities and Bonding Mechanisms in Stoichiometric
40 and Substoichiometric Molybdenum Carbide. *J. Appl. Phys.* **1999**, 86, 3758–3767.
41
42
43
44 (30) Kurlov, A. S.; Gusev, A. I. Tungsten Carbides and W-C Phase Diagram. *Inorg. Mater.* **2006**,
45 42, 121–127.
46
47
48
49 (31) Sugiyama, T.; Masuhara, H. Laser-Induced Crystallization and Crystal Growth. *Chem. - An*
50 *Asian J.* **2011**, 6, 2878–2889.
51
52
53 (32) Shi, Y.; Zhang, Y. Simulation of Random Packing of Spherical Particles with Different Size
54 Distributions. *Appl. Phys. A* **2008**, 92, 621–626.
55
56
57
58
59
60

- 1
2
3 (33) Ledbetter, H. M.; Naimon, E. R. Elastic Properties of Metals and Alloys. II. Copper. *J. Phys. Chem. Ref. Data* **1974**, *3*, 897–935.
4
5
6
7
8 (34) Okoli, S.; Haubner, R.; Lux, B. Carburization of Tungsten and Tantalum Filaments during
9 Low-Pressure Diamond Deposition. *Surf. Coatings Technol.* **1991**, *47*, 585–599.
10
11
12 (35) Kruth, J.; Mercelis, P.; Van Vaerenbergh, J.; Froyen, L.; Rombouts, M. Binding
13 Mechanisms in Selective Laser Sintering and Selective Laser Melting. *Rapid Prototyp. J.*
14 **2005**, *11*, 26–36.
15
16
17
18 (36) Kumar, S. Selective Laser Sintering/Melting. In *Comprehensive Materials Processing*;
19 Elsevier, Ltd., 2014;10, pp 93–134.
20
21
22
23 (37) Murr, L. E.; Gaytan, S. M.; Ramirez, D. A.; Martinez, E.; Hernandez, J.; Amato, K. N.;
24 Shindo, P. W.; Medina, F. R.; Wicker, R. B. Metal Fabrication by Additive Manufacturing
25 Using Laser and Electron Beam Melting Technologies. *J. Mater. Sci. Technol.* **2012**, *28*, 1–
26 14.
27
28
29
30
31 (38) Rafi, H. K.; Karthik, N. V.; Gong, H.; Starr, T. L.; Stucker, B. E. Microstructures and
32 Mechanical Properties of Ti6Al4V Parts Fabricated by Selective Laser Melting and Electron
33 Beam Melting. *J. Mater. Eng. Perform.* **2013**, *22*, 3872–3883.
34
35

TOC

